

Modeling the spatial control over point defect spin states via processing variables

Cite as: J. Appl. Phys. 129, 225703 (2021); doi: 10.1063/5.0039972

Submitted: 8 December 2020 · Accepted: 4 May 2021 ·

Published Online: 11 June 2021



Preston C. Bowes, Yifeng Wu, Jonathon N. Baker, and Douglas L. Irving^{a)}

AFFILIATIONS

Department of Materials Science and Engineering, North Carolina State University, Raleigh, North Carolina 27695, USA

^{a)}Author to whom correspondence should be addressed: dliirving@ncsu.edu

ABSTRACT

Contemporary models that are used to search for solid-state point defects for quantum-information applications tend to focus on the defect's intrinsic properties rather than the range of conditions in which they will form. In this work, a first-principles based multi-scale device model is used to explore how the conditions (i.e., growth temperature, doping concentration, unintentional impurity concentration) influence the formation of a neutral aluminum vacancy complexed with an oxygen impurity at a neighboring nitrogen site $v_{\text{Al}}\text{-}1\text{O}_{\text{N}}$ in an Si/Mg:AlN homojunction. Varying the donor (Si) concentration is predicted to lead to the greatest change in both the maximum height and shape of the $(v_{\text{Al}}\text{-}1\text{O}_{\text{N}})^0$ profile. The shape is found to depend on the acceptor (Mg) concentration as well, and a critical ratio between the acceptor and unintentional impurities below which the $(v_{\text{Al}}\text{-}1\text{O}_{\text{N}})^0$ center would not form was identified. A detailed analysis of the electrostatic potential, electric field, and defect chemistry obtained with the model was used to reveal the underlying causes of these changes. These results show the potential of varying processing parameters to manipulate the local electronic structure as a means to control the properties of point defects for quantum-information applications.

Published under an exclusive license by AIP Publishing. <https://doi.org/10.1063/5.0039972>

I. INTRODUCTION

Contemporary models seeking solid-state point defects for quantum-information applications have made great progress in identifying defects with useful characteristics,^{1–3} but evaluating the range of conditions in which they may be realized in a device remains a considerable challenge. Predicting such a range is necessary to efficiently explore the multi-dimensional space of processing variables and to ensure a desired profile that will be tolerant to minor changes encountered in commercial production. Existing device models have been instrumental in understanding the control of the charge states of point defects in diamond and SiC.^{4–9} Such models treat the defect chemistry parametrically in terms of general donor-type and/or acceptor-type dopants whose properties are fit to measured values. A device model that considers the detailed defect chemistry for each dopant may provide a deeper understanding of this control.

Recently, we presented a model for predicting the concentrations of point defects within the space charge region formed at thermal equilibrium in the vicinity of a homojunction.¹⁰ This model addresses the issue that often occurs in the range of Fermi levels where point defects readily form in equilibrium in an

undesirable spin configuration. For Fermi levels where the desirable spin configuration would form, the point defects do not readily form. This issue is common between candidate point defects in diamond,^{11–18} SiC,^{7,19} and AlN.^{1–3} In our prior work, the aluminum vacancy complexed with an oxygen impurity at a neighboring nitrogen site $v_{\text{Al}}\text{-}1\text{O}_{\text{N}}$, which we will refer to here as the OVAL center, was used as an example to highlight the model's potential.

Ultimately, Fermi was predicted to only form in conditions where the Fermi level (μ_e) pinned closer to the conduction band (CB) as its formation energy is high relative to other defects outside of these conditions.¹⁰ In these conditions in the absence of a space charge, OVAL formed in its -2 charge state, which is not useful for quantum applications. As a potential solution, a Si:AlN/Mg:AlN homojunction with uniform C and O background impurities was simulated with our model. The results indicated that the desired neutral state may form in high concentrations in a region 6 nm from the interface in the Si-doped side as a result of reionization in the presence of a space charge layer. In the same work, the variation of the OVAL⁰ profile with respect to the concentrations of Mg, Si, C, and O, the growth temperature, and the availability of nitrogen was briefly discussed, but the details of the

variation were not explored. This work aims to expand on this discussion and provides a predictive method for evaluating engineering strategies to control the localization of point defect spin states for quantum-information applications. Note that the model presented previously and in this work does not account for inter-diffusion of Mg and Si, which would otherwise affect the exact concentrations and distribution of defects predicted to form in the near interface region. If inter-diffusion of these dopants in AlN is substantial, the results would potentially be more qualitative. Thus, this paper explores how the charge states of defects vary in the vicinity of a chemically abrupt interface in a np-homojunction.

II. METHODS

Details of the device model and the DFT calculations used as inputs are mostly identical to those presented before^{10,20,21} and are summarized here for completeness. For each set of growth parameters, the equilibrium defect chemistry was calculated at the growth temperature (1400 K, unless otherwise noted) by self-consistently solving for the Fermi level μ_e and impurity chemical potentials μ_i in the system of equations given in Eq. (1). At the growth conditions, Eq. (1a) is set to 0 to satisfy the condition of charge neutrality, and a version of Eq. (1b) is written for each impurity with $[I]$ set to the desired incorporation concentration. In Eq. (1b), n_i is the number of atoms of impurity I in defect D^q .

In the dilute-approximation, the concentration of each defect $[D^q]$ is calculated from a Maxwell-Boltzmann distribution by Eq. (1c), where N_s is the number of lattice sites a defect can occupy, N_c is the number of symmetrically equivalent configurations, $E_{D^q}^{f,eq}$ is the equilibrium defect formation energy, k_B is Boltzmann's constant, and T is the temperature. Both N_s and N_c contribute to the configurational entropy associated with each symmetrically unique defect. The concentrations of electrons n and holes p in Eqs. (1d) and (1e) are also calculated from a Maxwell-Boltzmann distribution, where E_g is the bandgap and the prefactors are the effective density of states (DoS) computed from the effective DoS carrier masses ($m_e^* = 0.42$ and $m_h^* = 1.86$) derived from parabolic fits to the DFT band structure. The use of Maxwell-Boltzmann statistics is sufficient here since μ_e is at least $8k_B T$ and $24k_B T$ away from the valence and conduction bands, respectively, in all cases,

$$\rho = \sum_{D,q} q[D_{eq}^q] - n_{eq} + p_{eq}, \quad (1a)$$

$$[I] = \sum_{D,q} n_i[D_{eq}^q], \quad (1b)$$

$$[D_{eq}^q] = N_s N_c \exp\left(-\frac{E_{D^q}^{f,eq}}{k_B T}\right), \quad (1c)$$

$$n_{eq} = 2 \left(\frac{m_e^* k_B T}{2\pi\hbar^2}\right)^{3/2} \exp\left(-\frac{E_g - \mu_e}{k_B T}\right), \quad (1d)$$

$$p_{eq} = 2 \left(\frac{m_h^* k_B T}{2\pi\hbar^2}\right)^{3/2} \exp\left(-\frac{\mu_e}{k_B T}\right), \quad (1e)$$

$$E_{D^q}^{f,eq} = E_{D^q}^{\text{tot}} - E_{\text{bulk}}^{\text{tot}} - \sum_i n_i \mu_i + q\mu_e + E_{D^q}^{\text{corr}}. \quad (1f)$$

This system of equations is linked through the dependence of $E_{D^q}^{f,eq}$ on μ_e (taken relative to the DFT valence band E_v) and μ_i as shown in Eq. (1f), where $E_{D^q}^{\text{tot}}$ and $E_{\text{bulk}}^{\text{tot}}$ are the DFT total energies of the defective and pristine bulk supercells, respectively, and $E_{D^q}^{\text{corr}}$ is a finite-size correction based on the method of Kumagai and Oba²² using a measured relative permittivity of 9.14.²³ The values for $E_{D^q}^{\text{tot}}$ and $E_{\text{bulk}}^{\text{tot}}$ were extracted from hybrid functional DFT calculations of the defective and pristine supercells using the HSE06^{24,25} functional in VASP^{26–29} with an exact exchange amount of $\alpha = 0.32$, 96-atom supercells, a $2 \times 2 \times 2$ k-point mesh, and a kinetic energy cutoff of 520 eV.

The calculations of all but the Mg-related defects have been analyzed in-depth in prior works.^{20,30–32} In total, 602 charged defects were considered in the model to account for intrinsic and C-, O-, Si-, and Mg-related defects and are listed in Table I. Formation energies of relevant defects from this set are provided in Figs. S1–S3 in the supplementary material. The challenge of managing such a large number of simulations over time and across multiple students was mitigated by using a point defect informatics framework.³³

Defect concentrations calculated at the growth temperature were used to obtain the carrier concentrations and distribution of charged defects at room temperature by self-consistently solving for reionization among frozen in concentrations of the point defects. These reionized concentrations are used as input to the continuum model described by the system of equations in Eq. (2),

$$\nabla^2 \Phi = \frac{\rho}{\epsilon_0 \epsilon_r}, \quad (2a)$$

$$\rho = \sum_{D,q} q[D^q] - n + p, \quad (2b)$$

$$n = n_{eq} \exp\left(\frac{q_e \Phi}{k_B T}\right), \quad (2c)$$

$$p = p_{eq} \exp\left(-\frac{q_e \Phi}{k_B T}\right), \quad (2d)$$

$$[D^q] = [D_{eq}^q] \exp\left(-\frac{qq_e \Phi}{k_B T}\right). \quad (2e)$$

In Eq. (2), Φ is the electrostatic potential in V, ρ is the charge density that is now a function of Φ , ϵ_0 is the permittivity of the free space, and ϵ_r is the relative permittivity of wurtzite-AlN. It was assumed that the material is linear and isotropic allowing ϵ_r to be treated as a constant throughout the device. In Eq. (2b), $[D^q]$ represents the concentration of a defect with the formation energy perturbed by Φ , similar to the method used previously.^{34,35} The carrier concentrations were similarly updated from their equilibrium values.

TABLE I. Charged defects considered in the device model. A DX in the subscript represents a displaced defect, while the letter following DX indicates the direction of the displacement. For complexes like $(\text{V}_{\text{Al}}-\text{O}_{\text{N}})_{\text{a}}$ (i.e., OVAL_{a}), the subscript indicates where the 2-n members of the complexes were placed.

Defect	Charge	Defect	Charge	Defect	Charge	Defect	Charge
Al_{N}	-4..4	$\text{Si}_{\text{Al}}, \text{DX}-\text{Nc}$	-4..0, 2..4	$(\text{Si}_{\text{Al}}-\text{V}_{\text{N}})_{\text{a}}$	-3..3	$(\text{V}_{\text{Al}}-3\text{Si}_{\text{Al}})_{\text{a}}$	0..3
C_{Al}	-4..4	$\text{Si}_{\text{Al}}, \text{DX}-\text{a}$	-2..0	$(\text{Si}_{\text{Al}}-\text{V}_{\text{N}})_{\text{c}}$	-3..3	$(\text{V}_{\text{Al}}-3\text{V}_{\text{N}})_{\text{a}}$	-3..3
$\text{C}_{\text{Al}}, \text{DX}-\text{a}$	-2..2	$\text{Si}_{\text{Al}}, \text{DX}-\text{c}$	-2, -1, 2	$(\text{V}_{\text{Al}}-\text{O}_{\text{N}})_{\text{a}}$	-3..3	$(\text{V}_{\text{Al}}-3\text{V}_{\text{N}})_{\text{c}}$	-3..3
$\text{C}_{\text{Al}}, \text{DX}-\text{c}$	-2..2	Si_{N}	-4..4	$(\text{V}_{\text{Al}}-\text{O}_{\text{N}})_{\text{c}}$	-3..3	$(\text{V}_{\text{Al}}-4\text{O}_{\text{N}})_{\text{c}}$	-3..3
C_{N}	-4..4	$\text{Si}_{\text{N}}, \text{DX}-\text{a}$	-2..2	$(\text{V}_{\text{Al}}-1\text{Si}_{\text{Al}})_{\text{a}}$	-3..1	$(\text{V}_{\text{Al}}-1\text{C}_{\text{N}})_{\text{a}}$	-3..3
$\text{C}_{\text{N}}, \text{DX}-\text{a}$	-2, 1	$(\text{C}_{\text{Al}}-1\text{C}_{\text{N}})_{\text{a}}$	-3..3	$(\text{V}_{\text{Al}}-1\text{Si}_{\text{Al}})_{\text{c}}$	-3..1	$(\text{V}_{\text{Al}}-1\text{C}_{\text{N}})_{\text{c}}$	-3..3
Mg_{Al}	-4..4	$(\text{C}_{\text{Al}}-1\text{C}_{\text{N}})_{\text{c}}$	-3..3	$(\text{V}_{\text{Al}}-1\text{Si}_{\text{Al}})_{\text{c}} +$	-3..1	$(\text{V}_{\text{N}}-1\text{C}_{\text{N}})_{\text{a}}$	-2..2
Mg_{N}	-4..4	$(\text{C}_{\text{N}}-1\text{O}_{\text{N}})_{\text{a}}$	-2..2	$(\text{V}_{\text{Al}}-1\text{V}_{\text{N}})_{\text{a}}$	-3..3	$(\text{V}_{\text{N}}-1\text{C}_{\text{N}})_{\text{c}} +$	-2..2
N_{Al}	-4..4	$(\text{C}_{\text{N}}-1\text{O}_{\text{N}})_{\text{c}} +$	-2..2	$(\text{V}_{\text{Al}}-1\text{V}_{\text{N}})_{\text{c}}$	-3..3	$(\text{V}_{\text{N}}-1\text{C}_{\text{N}})_{\text{c}} -$	-2..2
O_{Al}	-4..4	$(\text{C}_{\text{N}}-1\text{O}_{\text{N}})_{\text{c}} -$	-2..2	$(\text{V}_{\text{Al}}-2\text{O}_{\text{N}})_{\text{a}}$	-3..3	$(\text{V}_{\text{N}}-1\text{O}_{\text{N}})_{\text{a}}$	-2..2
$\text{O}_{\text{Al}}, \text{DX}-\text{a}$	-2, 1, 2	$(\text{Si}_{\text{Al}}-1\text{C}_{\text{N}})_{\text{a}}$	-3..3	$(\text{V}_{\text{Al}}-2\text{O}_{\text{N}})_{\text{c}}$	-3..3	$(\text{V}_{\text{N}}-1\text{O}_{\text{N}})_{\text{c}} +$	-2..2
$\text{O}_{\text{Al}}, \text{DX}-\text{c}$	1, 2	$(\text{Si}_{\text{Al}}-1\text{C}_{\text{N}})_{\text{c}}$	-3..3	$(\text{V}_{\text{Al}}-2\text{Si}_{\text{Al}})_{\text{b}}$	-1..2	$(\text{V}_{\text{N}}-1\text{O}_{\text{N}})_{\text{c}} -$	-2..2
O_{N}	-4..4	$(\text{Si}_{\text{Al}}-2\text{C}_{\text{N}})_{\text{a}}$	-3..3	$(\text{V}_{\text{Al}}-2\text{V}_{\text{N}})_{\text{a}}$	-3..3	V_{Al}	-4..4
$\text{O}_{\text{N}}, \text{DX}-\text{a}$	-2, -1	$(\text{Si}_{\text{Al}}-2\text{C}_{\text{N}})_{\text{c}}$	-3..3	$(\text{V}_{\text{Al}}-2\text{V}_{\text{N}})_{\text{c}}$	-3..3	V_{N}	-4..4
$\text{O}_{\text{N}}, \text{DX}-\text{c}$	-2..0	$(\text{Si}_{\text{Al}}-1\text{O}_{\text{N}})_{\text{a}}$	-3..3	$(\text{V}_{\text{Al}}-3\text{O}_{\text{N}})_{\text{a}}$	-3..3		
Si_{Al}	-4..4	$(\text{Si}_{\text{Al}}-1\text{O}_{\text{N}})_{\text{c}}$	-3..3	$(\text{V}_{\text{Al}}-3\text{O}_{\text{N}})_{\text{c}}$	-3..3		

^aSimulated in 42 symmetrically unique configurations.^bSimulated in 13 symmetrically unique configurations.

In the simulated homojunction, Eq. (2) was solved for Φ numerically under the condition that $\nabla\Phi = 0$ at the ends of the simulation domain using FEniCS 2019.1.0.^{36–43} To ensure that the material returned to its bulk state far from the interface in each simulated processing condition, the total device length was extended to $400\text{ }\mu\text{m}$ from the $5.5\text{ }\mu\text{m}$ used in the original study. This increase in length was accompanied by an increase in the bulk node spacing to 100 nm and a reduction in both the width and node spacing of the interface region to 100 nm and $1\text{ }\text{\AA}$, respectively. As the values addressed in this work lose their physical meaning on the shorter length scale, the quantities plotted in the results were binned into 1 nm regions.

Values for the concentrations of Si, Mg, C, and O and the growth temperature T_{G} used in the original work are provided in the 2nd column of Table II. Each parameter was varied independently through 100 values between the minimums and maximums in the 3rd and 4th columns using a logarithmic scale for the dopant/impurity concentrations and a linear scale for the growth temperature. In the case of Si and Mg, the concentration was only varied in one half of the junction, while the concentrations of C

and O were varied uniformly throughout. As in the original work, the distributions of the dopants were assumed to be homogeneous with the concentrations of Si and Mg cutoff abruptly at the interface. The availability of nitrogen was not varied as it was found to only have a minor influence on the OVAL^0 profile in our prior work.¹⁰

III. RESULTS AND DISCUSSION

Before discussing any results, it is important to mention that the magnitude of the integrated areal charge density over the simulation domain was found to not exceed $1.40 \times 10^4\text{ e/cm}^2$ in all cases. While it is greater than the integrated areal charge density in our prior work, this value is still essentially 0. Increasing the mesh density in the bulk of the device by reducing the node spacing was neither found to have a significant impact on the integrated areal charge density nor the results discussed in this section. Additionally, though the OVAL center has two symmetrically unique configurations, the a -configuration is generally more stable and will be the focus of this discussion. Similar trends are observed for the c -configuration albeit at lower total concentrations.

A. Control with an acceptor dopant (Mg)

The predicted OVAL^0_{a} distribution as a function of Mg concentration is shown in Fig. 1. All figures presented in this work have the Si-doped portion of the device on the left and Mg on the right with the interface in the center at $x = 0$. In this case, the initial total concentration of the OVAL center (in the -2 charge state) in the Si-doped bulk remains constant because the Mg concentration is only changed in the right half of the device. This constant bulk concentration of $\text{OVAL}^{-2}_{\text{a}}$ is reflected in the constant maximum value of OVAL^0_{a} near the interface (bright yellow) in Fig. 1.

TABLE II. Model parameters with original values and range investigated. Si and Mg were varied over 60 gradations between the minimum and maximum values, while all other parameters were varied over 100 gradations.

Name	Original	Min	Max	Units
Si	10^{19}	10^{16}	10^{19}	cm^{-3}
Mg	10^{19}	10^{16}	10^{19}	cm^{-3}
C	10^{17}	10^{15}	10^{19}	cm^{-3}
O	5×10^{17}	10^{15}	10^{19}	cm^{-3}
T_{G}	1400	1100	1800	K

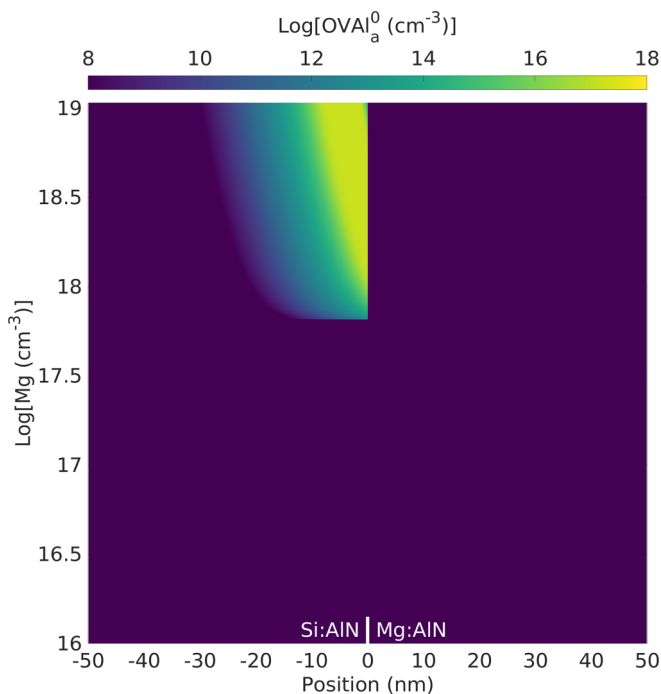


FIG. 1. Concentration of the OVAL_a^0 center as a function of Mg concentration and position, with the interface at the origin of the x axis.

This maximum occurs in conditions where Φ bends the bands just enough near the interface on the Si-doped side of the junction for the normally -2 center to transfer two electrons to the CB. This condition is met for Mg concentrations above approximately 10^{18} cm^{-3} as shown in Fig. 2(a). Below this Mg concentration, the background concentrations of O and C take over and push μ_e near $1.8\text{--}2 \text{ eV}$ and then near 5.3 eV above the valence band in the Mg-doped bulk as Mg falls below $2 \times 10^{17} \text{ cm}^{-3}$, which is well below the level of the unintentional oxygen donor concentration of $5 \times 10^{17} \text{ cm}^{-3}$. At these levels, the difference between μ_e in the bulk regions of the Si and Mg-doped halves is too small to yield a sufficient bending of the bands as shown in Fig. 2(b).

Adding Mg beyond 10^{18} cm^{-3} enhances the magnitude of the positive space charge region formed on the Mg-doped side of the interface as it continues to act as a deep acceptor at high concentrations. This increases the magnitude of the electric field in the interface region, as shown in Fig. S4 of the [supplementary material](#), which allows the field to penetrate further into the Si-doped half. As a result, the stability region outlined in Fig. 2(a) moves slightly further into the Si-doped half, which shifts the peak of the OVAL_a^0 distribution away from the interface in Fig. 1.

B. Control with a donor dopant (Si)

In varying the Si concentration and all other parameters discussed from here on in the paper, the analysis is further complicated by the dependence of the total initial OVAL_a concentration

on the parameter. This effect is most evident in the case of varying the concentration of Si, which also yields the greatest variation in the OVAL_a^0 profile as shown in Fig. 3. In addition to moving the profile peak tens of nanometers into the Si-doped half, reducing the Si concentration lowers the height of the peak. To provide more insight into this lowering of the peak, the bulk defect chemistry is shown as a function of Si concentration in Fig. 4.

In Fig. 4, unique configurations have been collapsed to single defects to aid in readability. Over most of the range, Si incorporates as Si_{Al}^1 and acts as a donor. At higher concentrations, Si begins to form complexes of $(\text{V}_{\text{Al}}-2\text{Si}_{\text{Al}})^{-1}$ and $(\text{V}_{\text{Al}}-3\text{Si}_{\text{Al}})^0$ in a form of self-compensation described in detail by Harris *et al.*²⁰ The defects formed by O undergo a similar series of transitions as the concentration of Si is reduced and O and C take over as the primary dopants. For Si above roughly 10^{18} cm^{-3} O incorporates primarily as $(\text{V}_{\text{Al}}-1\text{O}_{\text{N}})^{-2}$. Below this concentration, $(\text{V}_{\text{Al}}-2\text{O}_{\text{N}})^{-1}$ takes over for the two member complex, but $(\text{V}_{\text{Al}}-1\text{O}_{\text{N}})^{-2}$ is still present above 10^{16} cm^{-3} until Si approaches $2 \times 10^{17} \text{ cm}^{-3}$. Here, the four member complex $(\text{V}_{\text{Al}}-3\text{O}_{\text{N}})^0$ is the dominant form of O incorporation, and the concentration of the two member complex falls below 10^{16} cm^{-3} . The reduction in the peak height of the OVAL_a^0 center in Fig. 4 coincides with the drop in the initial concentration of the two member complex in the bulk defect chemistry.

The region in which the neutral charge state is stabilized can be understood in terms of the local electrostatic potential provided in Fig. 5. In Fig. 5, the magenta and cyan lines represent isocontours where Φ equals the $(-1|0)$ and $(0|1)$ thermodynamic transition levels of the OVAL_a center at 300 K. The region bound by these isocontours directly lines up with the high concentration region of the neutral OVAL_a center in Fig. 3. As the Si concentration is reduced, the junction's built-in potential increases slightly from 5.04 to 5.11 V around $[\text{Si}] = 10^{18} \text{ cm}^{-3}$ and then decreases to 4.72 V at 10^{16} cm^{-3} . This has a large effect on the local electric field near the interface, as shown in Fig. S5 of the [supplementary material](#), which widens the stability window of the OVAL_a^0 center by hundreds of nanometers at the lowest Si concentration. Conversely, increasing the Si concentration leads to an increase in the magnitude of the electric field, which narrows the stability window and causes the field to extend deeper into the Mg-doped half of the junction, which is the inverse of the effect observed on increasing the Mg concentration. This is expected since Si acts as a donor and Mg an acceptor.

C. Control with minority impurities (C and O)

Like Si, changing the concentration of C leads to changes in the bulk concentration of OVAL_a^{-2} , but since it is varied throughout the junction, it also changes the defect chemistry in Mg-doped half and thus the reference level for the thermodynamic transition levels of the center. Despite this complexity, the overall change observed in the OVAL_a^0 profile is minor as shown in Fig. 6. The overall peak height and position do not change, but the profile is broadened slightly at high C concentrations before a sharp drop-off at 10^{19} cm^{-3} . The broadening is a result of C gradually reducing the built-in potential in the junction by compensating for Si_{Al}^1 on the Si-doped side and $\text{Mg}_{\text{Al}}^{-1}$ on the Mg-doped side, which pulls the bulk Fermi level closer to midgap. By reducing the built-in potential,

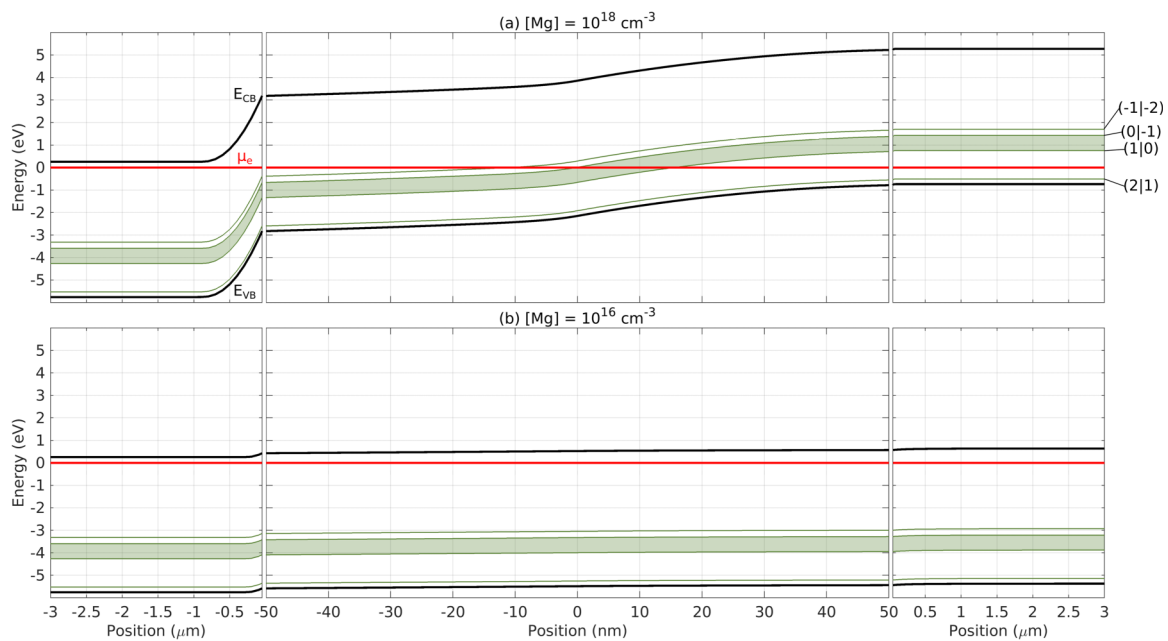


FIG. 2. Band diagrams of the homojunction with the OVA_a thermodynamic transition levels at two separate Mg concentrations: (a) 10^{18} cm^{-3} and (b) 10^{16} cm^{-3} . The shaded region represents the stability window of the neutral charge state.

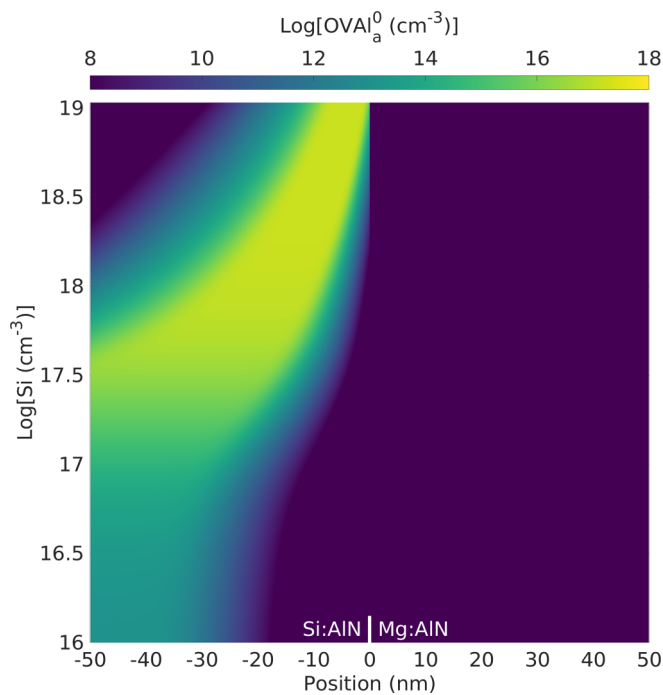


FIG. 3. Concentration of the OVA_a center as a function of Si concentration and position, with the interface at the origin of the x axis.

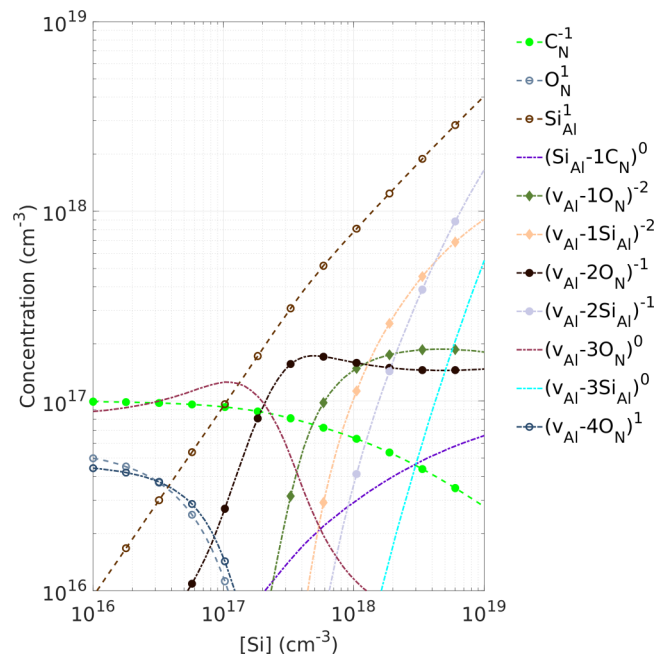


FIG. 4. Bulk defect concentrations as a function of Si concentration for AlN with C at 10^{17} cm^{-3} and O at $5 \times 10^{17} \text{ cm}^{-3}$ grown at 1400 K and quenched to 300 K.

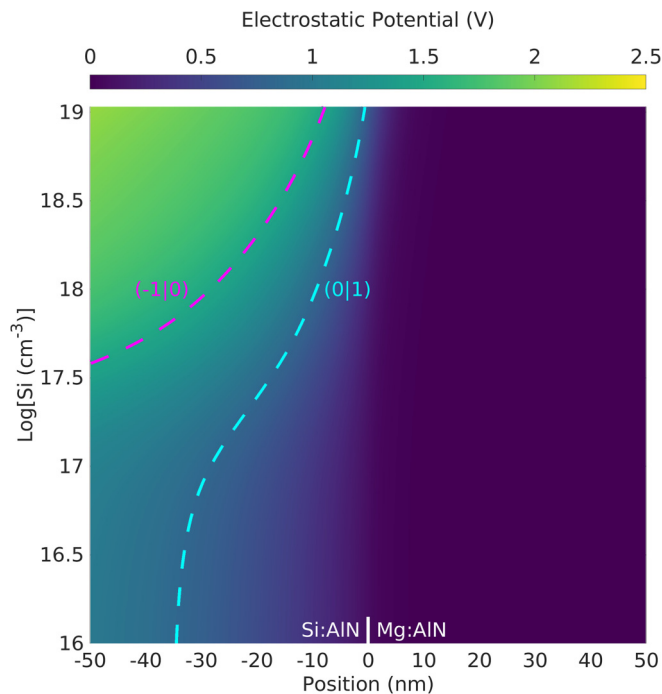


FIG. 5. Electrostatic potential Φ as a function of Si concentration and position, with the interface at the origin of the x axis. The magenta and cyan lines represent isocontours where Φ equals the $(-1|0)$ and $(0|1)$ thermodynamic transition levels of the OVAI_a center at 300 K relative to $\mu_e = 0.66$ eV.

the magnitude of the electric field decreases and spreads further into each half of the junction, which extends the stability region of the OVAI_a^0 center into the Si-doped half. The sharp drop-off in the concentration of the OVAI_a^0 center near 10^{19} cm^{-3} is a continuation of this trend where C now effectively compensates for Mg and μ_e is pushed above the $(0|-1)$ transition of the OVAL center.

Varying the concentration of O as seen in Fig. 7 yields changes to the maximum of the OVAI_a^0 distribution but does not alter its shape significantly. The OVAI_a^0 concentration increases from roughly 10^{15} cm^{-3} at the same concentration of O to $4 \times 10^{17} \text{ cm}^{-3}$ for O just under 10^{19} cm^{-3} . This is due to an identical change in the bulk concentration of OVAI_a^{-2} with the O concentration. Despite this significant change in the OVAI_a^{-2} concentration, the bulk Fermi level in the Si-doped side remains relatively constant as much of the oxygen is trapped in complexes, which prevent it from compensating for the Si present. On the Mg-doped side, no aluminum vacancies are present to form complexes and O is able to more effectively compensate for Mg. This leads to an increase in μ_e in the Mg-doped side above the $(0|-1)$ transition of the OVAL center for O near 10^{19} cm^{-3} which prevents any OVAI_a^0 from forming.

D. Control with the growth temperature

Modifying the growth temperature from 1400 K used previously while holding total impurity concentrations fixed (an exploration of a complex redistribution with growth temperature) leads

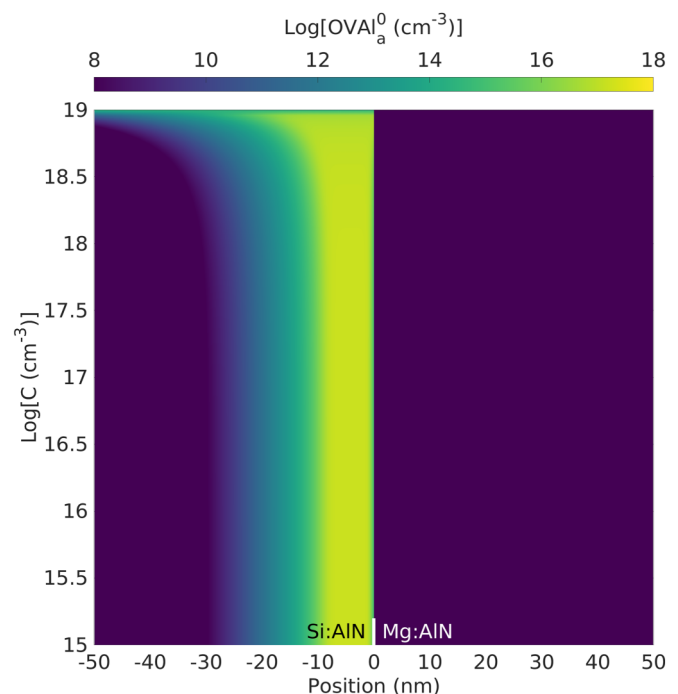


FIG. 6. Concentration of the OVAI_a^0 center as a function of C concentration and position, with the interface at the origin of the x axis.

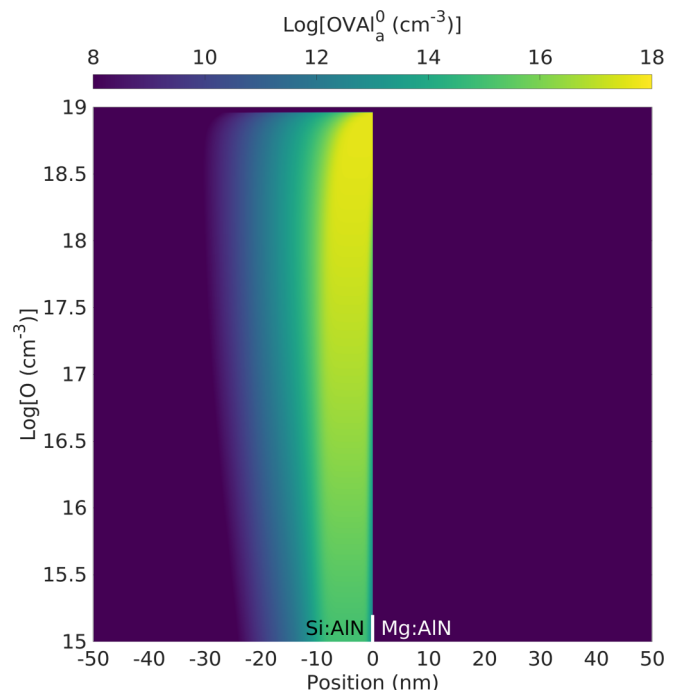


FIG. 7. Concentration of the OVAI_a^0 center as a function of O concentration and position, with the interface at the origin of the x axis.

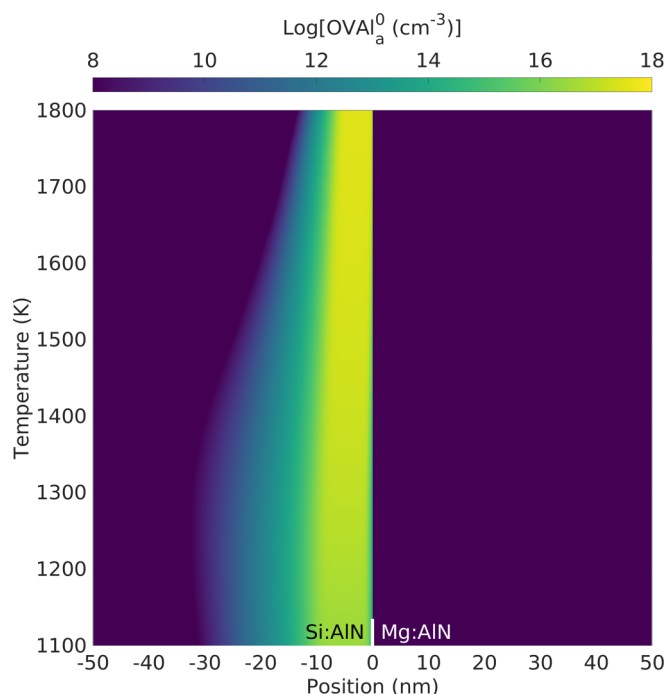


FIG. 8. Concentration of the OVAI_a^0 center as a function of growth temperature and position, with the interface at the origin of the x axis.

to changes in the maximum of the OVAI_a^0 distribution and its shape, as shown in Fig. 8. However, the change in the maximum is slight compared to that predicted for varying the O concentration with OVAI_a^0 ranging from 3×10^{16} to $4 \times 10^{17} \text{ cm}^{-3}$ from 1100 to 1800 K. This change is again identical to changes in the bulk concentration of OVAI_a^{-2} with the growth temperature. The broadening of the distribution at lower growth temperatures is a result of reducing the built-in potential of the junction by altering the defect chemistry throughout the device similar to the mechanism discussed for increasing the C concentration. Only instead of introducing more compensating defects, reducing the growth temperature decreases the concentration of Si_{Al}^1 as more of it complexes with V_{Al} as $(\text{V}_{\text{Al}}-3\text{Si}_{\text{Al}})^0$ on the Si-doped side and increases the concentrations of $\text{Mg}_{\text{Al}}^{-1}$ and V_{N}^4 at the same rate on the Mg-doped side.

IV. CONCLUSIONS

Starting from hybrid functional DFT calculations of point defect formation energies, this work demonstrates not only the level of control one can have over the spatial distribution of the OVAI_a^0 center through varying processing parameters in AlN, but also the breadth and depth of information that can be obtained with comprehensive multi-scale device models. The results presented indicate that the height and shape of the OVAI_a^0 distribution can be tuned by varying the concentrations of the majority donor (Si) and acceptor (Mg) dopants, minority (C and O) impurities, and the growth temperature.

Altering the Si concentration yielded the greatest variation in terms of both the shape and height of the profile with the height controlled by the formation of OVAI_a^{-2} in the bulk and shape being a property of the magnitude and distribution of the local electric field. For Mg, no OVAI_a^0 was found to form if the Mg concentration fell below that of the background concentrations of C and O, and increasing the Mg content pushed the maximum of the OVAI_a^0 distribution further into the Si-doped half of the junction. In contrast, C, O, and the growth temperature had only a minor influence on the shape of the OVAI_a^0 distribution. In the case of C, the height was also relatively invariant until its concentration approached that of Si and Mg where no OVAI_a^0 formed. The concentration of O had a more direct impact on the height of the profile but little impact on its shape and exhibited a cutoff at high concentrations similar to C. Conversely, the growth temperature had a minor impact on the height of the distribution and a larger impact on how quickly the concentration of OVAI_a^0 decreased away from the interface.

Additional work is needed to explicitly address varying multiple parameters simultaneously, as well as diffusion of the defects in the vicinity of the interface at the growth temperature, but the results presented here can serve as an initial guide for fabricating devices with a desired profile of OVAI_a^0 centers. The model presented is also generally applicable to any material system with a sufficient database of first-principle's point defect calculations. Overall, our results show the possibilities of tuning processing parameters to alter the local electronic structure as a means to control the properties of point defects for quantum-information applications.

Furthermore, various authors recently demonstrated electrical control over an optically active center in an SiC device.^{7,8} This process can be explained with a variety of available semiconductor simulation software packages by fitting the densities of acceptors and donors and their respective compensation ratios to the measured device properties.^{4,8} The model presented in this work may be extended to further explore the non-equilibrium conditions studied by these authors and provide additional insight on the influence of the applied bias on the detailed defect chemistry of AlN.

SUPPLEMENTARY MATERIAL

See the [supplementary material](#) for additional information on the formation energy diagrams for defects that are found to occur in significant concentrations. In addition, further contours are given for the electric fields in the near interface region.

ACKNOWLEDGMENTS

P. C. Bowes was supported by the Department of Defense through the National Defense Science & Engineering Graduate (NDSEG) fellowship program. Computational methods were developed with financial support from the Air Force Office of Scientific Research (AFOSR) (Nos. FA9550-14-1-0264 and FA9550-17-1-0318) and the National Science Foundation (NSF) (No. DMR-1151568). Computer time for the DFT calculations was provided by DoD HPCMP and NCSU HPC. Professors Zlatko Sitar and Ramón Collazo are acknowledged for their feedback and discussions on unintentional impurities in AlN.

DATA AVAILABILITY

Numerical details of DFT (e.g., HSE exchange amount and kinetic energy cutoff) and finite element simulations (e.g., system of equations and boundary conditions) that are required to generate the present results are discussed in Sec. II. The data that support the findings of this study are available from the corresponding author upon reasonable request.

REFERENCES

- ¹Y. Tu, Z. Tang, X. G. Zhao, Y. Chen, Z. Q. Zhu, J. H. Chu, and J. C. Fang, *Appl. Phys. Lett.* **103**, 072103 (2013).
- ²J. B. Varley, A. Janotti, and C. G. Van De Walle, *Phys. Rev. B* **93**, 161201 (2016).
- ³H. Seo, M. Govoni, and G. Galli, *Sci. Rep.* **6**, 20803 (2016).
- ⁴D. Y. Fedyanin and M. Agio, *New J. Phys.* **18**, 073012 (2016).
- ⁵M. Pfender, N. Aslam, P. Simon, D. Antonov, G. Thiering, S. Burk, F. Fávoro de Oliveira, A. Denisenko, H. Fedder, J. Meijer, J. A. Garrido, A. Gali, T. Teraji, J. Isoya, M. W. Doherty, A. Alkauskas, A. Gallo, A. Grüneis, P. Neumann, and J. Wrachtrup, *Nano Lett.* **17**, 5931 (2017), pMID: 28872881.
- ⁶D. A. Broadway, N. Donschuk, A. Tsai, S. E. Lillie, C.-K. Lew, J. C. McCallum, B. Johnson, M. Doherty, A. Stacey, L. Hollenberg *et al.*, *Nat. Electron.* **1**, 502 (2018).
- ⁷C. P. Anderson, A. Bourassa, K. C. Miao, G. Wolfowicz, P. J. Mintun, A. L. Crook, H. Abe, J. Ul Hassan, N. T. Son, T. Ohshima, and D. D. Awschalom, *Science* **366**, 1225 (2019).
- ⁸M. Widmann, M. Niethammer, D. Y. Fedyanin, I. A. Khramtsov, T. Rendler, I. D. Booker, J. Ul Hassan, N. Morioka, Y.-C. Chen, I. G. Ivanov, N. T. Son, T. Ohshima, M. Bockstedte, A. Gali, C. Bonato, S.-Y. Lee, and J. Wrachtrup, *Nano Lett.* **19**, 7173 (2019), pMID: 31532999.
- ⁹K. Bray, D. Y. Fedyanin, I. A. Khramtsov, M. O. Bilokur, B. Regan, M. Toth, and I. Aharonovich, *Appl. Phys. Lett.* **116**, 101103 (2020).
- ¹⁰P. C. Bowes, Y. Wu, J. N. Baker, J. S. Harris, and D. L. Irving, *Appl. Phys. Lett.* **115**, 052101 (2019).
- ¹¹W. Gilpin, in *2012 NNIN REU Convocation* (2012), p. 202, available at https://www.nnin.org/sites/default/files/2012reu/2012nninREU_Gilpin.pdf.
- ¹²H. Kato, M. Wolfer, C. Schreyvogel, M. Kunzer, W. Müller-Sebert, H. Obloh, S. Yamasaki, and C. Nebel, *Appl. Phys. Lett.* **102**, 151101 (2013).
- ¹³T. W. Shanley, A. A. Martin, I. Aharonovich, and M. Toth, *Appl. Phys. Lett.* **105**, 063103 (2014).
- ¹⁴M. V. Hauf, P. Simon, N. Aslam, M. Pfender, P. Neumann, S. Pezzagna, J. Meijer, J. Wrachtrup, M. Stutzmann, F. Reinhard, and J. A. Garrido, *Nano Lett.* **14**, 2359 (2014).
- ¹⁵C. Schreyvogel, V. Polyakov, R. Wunderlich, J. Meijer, and C. E. Nebel, *Sci. Rep.* **5**, 12160 (2015).
- ¹⁶M. Shimizu, T. Makino, T. Iwasaki, J. Hasegawa, K. Tahara, W. Naruki, H. Kato, S. Yamasaki, and M. Hatano, *Diam. Relat. Mater.* **63**, 192 (2016).
- ¹⁷T. Murai, T. Makino, H. Kato, M. Shimizu, T. Murooka, E. D. Herbschleb, Y. Doi, H. Morishita, M. Fujiwara, M. Hatano, S. Yamasaki, and N. Mizuochi, *Appl. Phys. Lett.* **112**, 111903 (2018).
- ¹⁸M. Shimizu, T. Makino, T. Iwasaki, K. Tahara, H. Kato, N. Mizuochi, S. Yamasaki, and M. Hatano, *Appl. Phys. Exp.* **11**, 10 (2018).
- ¹⁹K. C. Miao, A. Bourassa, C. P. Anderson, S. J. Whiteley, A. L. Crook, S. L. Bayliss, G. Wolfowicz, G. Thiering, P. Udvarhelyi, V. Ivady, H. Abe, T. Ohshima, A. Gali, and D. D. Awschalom, *Sci. Adv.* **5**, eaay0527 (2019).
- ²⁰J. S. Harris, J. N. Baker, B. E. Gaddy, I. Bryan, Z. Bryan, K. J. Mirrielees, P. Reddy, R. Collazo, Z. Sitar, and D. L. Irving, *Appl. Phys. Lett.* **112**, 152101 (2018).
- ²¹J. N. Baker, P. C. Bowes, J. S. Harris, and D. L. Irving, *J. Appl. Phys.* **124**, 114101 (2018).
- ²²Y. Kumagai and F. Oba, *Phys. Rev. B* **89**, 195205 (2014).
- ²³A. T. Collins, E. C. Lightowlers, and P. J. Dean, *Phys. Rev.* **158**, 833 (1967).
- ²⁴J. Heyd, G. E. Scuseria, and M. Ernzerhof, *J. Chem. Phys.* **118**, 8207 (2003).
- ²⁵J. Heyd, G. E. Scuseria, and M. Ernzerhof, *J. Chem. Phys.* **124**, 219906 (2006).
- ²⁶G. Kresse and J. Hafner, *Phys. Rev. B: Condens. Matter Mater. Phys.* **47**, 558 (1993).
- ²⁷G. Kresse and J. Hafner, *Phys. Rev. B: Condens. Matter Mater. Phys.* **49**, 14251 (1994).
- ²⁸G. Kresse and J. Furthmüller, *Comput. Mater. Sci.* **6**, 15 (1996).
- ²⁹G. Kresse and J. Furthmüller, *Phys. Rev. B* **54**, 11169 (1996).
- ³⁰R. Collazo, J. Xie, B. E. Gaddy, Z. Bryan, R. Kirste, M. Hoffmann, R. Dalmau, B. Moody, Y. Kumagai, T. Nagashima, Y. Kubota, T. Kinoshita, A. Koukitu, D. L. Irving, and Z. Sitar, *Appl. Phys. Lett.* **100**, 191914 (2012).
- ³¹B. E. Gaddy, Z. Bryan, I. Bryan, R. Kirste, J. Xie, R. Dalmau, B. Moody, Y. Kumagai, T. Nagashima, Y. Kubota, T. Kinoshita, A. Koukitu, Z. Sitar, R. Collazo, and D. L. Irving, *Appl. Phys. Lett.* **103**, 161901 (2013).
- ³²B. E. Gaddy, Z. Bryan, I. Bryan, J. Xie, R. Dalmau, B. Moody, Y. Kumagai, T. Nagashima, Y. Kubota, T. Kinoshita, A. Koukitu, R. Kirste, Z. Sitar, R. Collazo, and D. L. Irving, *Appl. Phys. Lett.* **104**, 202106 (2014).
- ³³J. N. Baker, P. C. Bowes, J. S. Harris, and D. L. Irving, *MRS Commun.* **9**, 839 (2019).
- ³⁴J. Yang, M. Youssef, and B. Yildiz, *Phys. Chem. Chem. Phys.* **19**, 3869 (2017).
- ³⁵Y. Wu, P. C. Bowes, J. N. Baker, and D. L. Irving, *J. Appl. Phys.* **128**, 014101 (2020).
- ³⁶M. S. Alnaes, J. Blechta, J. Hake, A. Johansson, B. Kehlet, A. Logg, C. Richardson, J. Ring, M. E. Rognes, and G. N. Wells, *Arch. Num. Softw.* **3**, 9 (2015).
- ³⁷A. Logg, K.-A. Mardal, and G. Wells, *Automated Solution of Differential Equations by the Finite Element Method: The FEniCS Book* (Springer Science & Business Media, 2012), Vol. 84.
- ³⁸A. Logg and G. N. Wells, *ACM Trans. Math. Softw.* **37**(2), 20 (2010).
- ³⁹M. S. Alnaes, A. Logg, K. B. Oelgaard, M. E. Rognes, and G. N. Wells, *ACM Trans. Math. Softw.* **40**(2), 9 (2014).
- ⁴⁰K. B. Oelgaard and G. N. Wells, *ACM Trans. Math. Softw.* **37**(1), 8 (2010).
- ⁴¹M. S. Alnaes, A. Logg, K.-A. Mardal, O. Skavhuug, and H. P. Langtangen, *Int. J. Comput. Sci. Eng.* **4**, 231 (2009).
- ⁴²R. C. Kirby, *ACM Trans. Math. Softw.* **30**, 502 (2004).
- ⁴³R. C. Kirby and A. Logg, *ACM Trans. Math. Softw.* **32**, 417 (2006).